DISCONTINUOUS GALERKIN ISOGEOMETRIC ANALYSIS OF ELLIPTIC PROBLEMS ON SEGMENTATIONS WITH NON-MATCHING INTERFACES

Christoph Hofer[1], Ioannis Toulopoulos[1]

[1] *Johann Radon Institute for Computational and Applied Mathematics, Austrian Academy of Sciences, Altenbergerstr. 69, A-4040 Linz, Austria,*

Abstract

In this paper, we develop a discontinuous Galerkin Isogeometric Analysis method for solving elliptic problems on decompositions of the computational domain into volumetric patches with non-matching parametrized interfaces. We specially focus on high order numerical solutions for complex gap regions and extend ideas from our previous work on simple gap regions. For the communication of the numerical solution between the subdomains, which are separated by the gap region, discontinuous Galerkin numerical fluxes are constructed taking into account the diametrically opposite points on the boundary of the gap. Due to lack of information on the behavior of the solution in the gap region, the fluxes coming from the interior of the gap are approximated by Taylor expansions with respect to the adjacent subdomain solutions. We follow the same ideas of our previous work and show a priori error estimates in the dG-norm, with respect to the mesh size and the gap distance. Numerical examples, performed for two-, three- and even four-dimensional computational domains, demonstrate the robustness of the proposed numerical method and validate the estimates predicted by the theory.

Keywords: Elliptic diffusion problems, Heterogeneous diffusion coefficients, Isogeometric Analysis, Incorrect segmentation, non-matching parametrized interfaces, Multi-patch discontinuous Galerkin method.

---

1. Introduction

Isogeometric analysis (IgA) is a relatively new approach to the numerical solution of partial differential equations in which the finite dimensional spaces (B-splines, NURBS, T-spline etc.) used to approximate the solution are the same as those used to parameterize the computational domain [4]. In many practical applications, it is necessary to describe the computational domain with multiple subdomains, called also patches. For example, if different mathematical models are used in different parts of the domain, the numerical procedure is simplified by describing these parts as different subdomains (patches). Each subdomain is separately parametrized using the superior B-splines, NURBS or T-spline finite dimensional spaces, [4]. We can apply several segmentation techniques and procedures, for splitting complex domains into simpler subdomains, see, e.g., [10], [15], [7] , [17], for a discussion in isogeometric segmentation. The subdomain parametrizations are then constructed by defining the corresponding subdomain control net, see [4], and [9] for a more comprehensive analysis in surface representations. Usually, we obtain compatible parametrizations of the subdomains, meaning that using a relative coarse control mesh, the parameterizations of the adjoining subdomain interfaces are identical. However, some serious difficulties can arise, especially, when the subdomains differ topologically a lot from a cube. At the end of the segmentation procedure, we can have subdomain control nets, whose control points related to an interface may not appropriately match, resulting in a non-matching parametrized interface. In this case, gap regions can be created between the subdomains, where the boundary of the gap region is formed by parts of the boundary of the subdomains, see Fig. 1(a). An IgA approach for solving partial differential equations on non-matching parametrized interfaces has not previously been considered. Indeed, it is an important issue of the IgA framework to devise a stable numerical procedure that can successfully be applied to

---

☆

URL: `(christoph.hofer, ioannis.toulopoulos)@oeaw.ac.at@ricam.oeaw.ac.at` (Ioannis Toulopoulos)

this type of decompositions. The purpose of our previous paper [8] and of this paper is to formulate and to analyse a natural extension of discontinuous Galerkin (dG) IgA methods, see e.g., [13], to IgA decompositions with non-matching parametrized interfaces.

In [8], we initiated the development of a dG IgA method to solve a linear diffusion problems on decompositions with non-matching interface parametrizations. The main goal was to construct appropriate numerical fluxes on the non-matching interfaces, using values of the adjacent subdomain numerical solution. More precisely, at the beginning the gap is considered as a subdomain of the decomposition. Then, dG numerical fluxes are constructed on the common boundary parts of the subdomains and the gap, using the (unknown) normal fluxes coming from the interior of the gap region. Since these fluxes are not available, they are replaced by Taylor expansions with respect values of the adjacent subdomain solution. In particular, for every point on the gap boundary we define its corresponding diametrically opposite boundary point, see Fig. 1(b). The key idea is to use Taylor expansions to approximate the unknown normal fluxes on every point of the gap boundary, by means of the known subdomain solution values on the opposite point. We can say that the Taylor expansions are playing the role of a bridge for the communication between the solutions of the adjacent subdomains. In [8], we present the discretization error analysis and performed numerical tests, utilizing uni-axial Taylor expansions. In the present paper, we generalize this work to the case of general gap regions in any dimension by applying multi-directional Taylor expansions between the diametrically opposite points on the gap boundary. Then, as in [8], these expansions are used to construct appropriate dG numerical fluxes on the gap boundary in order to ensure the communication of the numerical solution of the subdomains which are separated by the gap.

For simplicity, we focus on the case where we have an initial decomposition of Ω consisting of two subdomains, where only one gap region, say Ω_g, appears between the two adjacent subdomain. This means that the domain decomposition is given by $\mathcal{T}_H(\Omega \setminus \overline{\Omega}_g) := \{\Omega_l, \Omega_r\}$, and $\overline{\Omega} = \overline{\Omega}_l \cup \overline{\Omega}_r \cup \overline{\Omega}_g$. The model problem that we study is a linear diffusion problem with discontinuous diffusion coefficient. Following the same ideas as in [8] for the uni-axial Taylor expansions, we show the same a priori error estimates in the classical dG-norm $\|.\|_{dG}$ for the current case of multi-directional Taylor expansions. As in [8], the estimates again are expressed in terms of the mesh size h and the distance d_g of the gap, which is a parameter which quantifies the maximum distance between two diametrically opposite points on $\partial\Omega_g$. The discretization error analysis is based on the results presented in [13] and [12], where dG IgA methods were analysed for the same diffusion problem with matching interface parametrizations. In particular, we show that, if the IgA space defined on subdomains Ω_i, $i = l, r$ has the approximation power h^k and the gap distance is $\mathcal{O}(h^{k+\frac{1}{2}})$, i.e. the flux approximation is of $\mathcal{O}(h^k)$, then we obtain optimal convergence rate for the error in the dG norm $\|.\|_{dG}$. In the special case where the gap distance is $\mathcal{O}(h)$, we obtain a reduced discretization error of order $\mathcal{O}(h^{\frac{1}{2}})$. The same estimates have been shown in [8] for the case of utilizing uni-axial Taylor expansions. Our proposed method has been successfully applied to the solution of the model problem on a wide range of different test cases confirming the theoretical estimates. All these test cases are discussed in the last Section of the manuscript.

We lastly mention that several techniques have been investigated recently for coupling non-matching (or non-conforming) subdomain parametrizations in some weak sense. In [18] and [16], Nitsche's method have been applied to enforce weak coupling conditions along trimmed B-spline patches. In [2], the most common techniques for imposing weakly the continuity of the solution on the interfaces have been applied and tested on nonlinear elasticity problems. The numerical tests have been performed on non-matching grid parametrizations. Furthermore, mortar methods have been developed in the IgA content utilizing different B-spline degrees for the Lagrange multiplier in [3]. The method has been applied for performing numerical tests on decompositions with non-matching interface parametrizations.

The paper is organized as follows. In Section 2, some notations, the weak form of the problem and the definition of the B-spline spaces are given. We further describe the gap region. In Section 3, we derive the problem in $\Omega \setminus \overline{\Omega}_g$, the approximation of the normal fluxes on the $\partial\Omega_g$, and the dG IgA scheme. In the last part of this section, we estimate the remainder terms in the Taylor expansion. Section 4 is devoted to the derivation of the a priori error estimates. Finally, in Section 5, we present numerical tests for validating the theoretical results on two-, three- and four- dimensional test problems. The paper closes with some conclusions in Section 6.

2. The model problem

2.1. Preliminaries

We start with some preliminary definitions and notations. Let Ω be a bounded Lipschitz domain in $\mathbb{R}^d$, $d = 2, 3$, and let $\alpha = (\alpha_1, ..., \alpha_d)$ be a multi-index of non-negative integers α_1,...,, α_d with degree

$|\alpha| = \sum_{j=1}^{d} \alpha_j$. For any α, we define the differential operator $D^\alpha = D_1^{\alpha_1} \cdots D_d^{\alpha_d}$, with $D_j = \partial/\partial x_j$, $j = 1, \dots, d$, and $D^{(0,\dots,0)}u = u$. For a non-negative integer m, let $C^m(\Omega)$ denote the space of all functions $\phi : \Omega \to \mathbb{R}$, whose partial derivatives $D^\alpha \phi$ of all orders $|\alpha| \leq m$ are continuous in Ω. We denote the subset of all functions from $C^\infty(\Omega)$ with compact support in Ω by $C_0^\infty(\Omega)$ (or $\mathcal{D}(\Omega)$). Let $1 \leq p < \infty$ be fixed and l be a non-negative integer. As usual, $L^p(\Omega)$ denotes the Lebesgue spaces for which $\int_\Omega |u(x)|^p \, dx < \infty$, endowed with the norm $\|u\|_{L^p(\Omega)} = \big(\int_\Omega |u(x)|^p \, dx \big)^{\frac{1}{p}}$, and $W^{l,p}(\Omega)$ is the Sobolev space, which consists of the functions $\phi : \Omega \to \mathbb{R}$ such that their weak derivatives $D^\alpha \phi$ with $|\alpha| \leq l$ belong to $L^p(\Omega)$. If $\phi \in W^{l,p}(\Omega)$, then its norm is defined by

$$\|\phi\|_{W^{l,p}(\Omega)} = \Big(\sum_{0 \leq |\alpha| \leq l} \|D^\alpha \phi\|^p_{L^p(\Omega)} \Big)^{\frac{1}{p}} \text{ and } \|\phi\|_{W^{l,\infty}(\Omega)} = \max_{0 \leq |\alpha| \leq l} \|D^\alpha \phi\|_{L^\infty(\Omega)}.$$

We refer to [1] for more details about Sobolev spaces.

2.2. The elliptic problem

Let Ω be a bounded Lipschitz domain in $\mathbb{R}^d$, $d = 2, 3$ which is assumed to consist (only for simplicity) of two Lipschitz subdomains Ω_1 and Ω_2 with common interface F, such that

$$\overline{\Omega} = \overline{\Omega}_1 \cup \overline{\Omega}_2, \quad \Omega_1 \cap \Omega_2 = \emptyset, \quad \overline{\Omega}_1 \cap \overline{\Omega}_2 = F. \tag{2.1}$$

For this decomposition, we use the notation $\mathcal{T}_H(\Omega) = \{\Omega_i\}_{i=1}^2$, and define the space

$$W^{l,2}(\mathcal{T}_H(\Omega)) = \{u \in L^2(\Omega) : u|_{\Omega_i} \in W^{l,2}(\Omega_i), \text{ for } i = 1, 2\}, \tag{2.2}$$

where $l \geq 0$ is an integer. We consider the following elliptic problem:

$$-\mathrm{div}(\rho \nabla u) = f \text{ in } \Omega \quad \text{and} \quad u = u_D \text{ on } \partial\Omega, \tag{2.3}$$

where f and u_D are given smooth data and the diffusion coefficient ρ is assumed to be positive constant on each subdomain, namely $\rho = \rho_i$ in Ω_i, for $i = 1, 2$. In what follows, u_i denotes the solution on each subdomain Ω_i, $i = 1, 2$.

The weak formulation of the boundary value problem (2.3) reads as follows: for given source function f and Dirichlet data u_D, find a function $u \in W^{1,2}(\Omega)$ such that $u = u_D$ on $\partial\Omega$ and satisfies the variational identity

$$a(u, \phi) = l_f(\phi), \ \forall \phi \in W_0^{1,2}(\Omega) = \{\phi \in W^{1,2}(\Omega) : \ \phi = 0 \text{ on } \partial\Omega\}, \tag{2.4}$$

where the bilinear form $a(\cdot, \cdot)$ and the linear form $l_f(\cdot)$ are defined by

$$a(u, \phi) = \int_\Omega \rho \nabla u \nabla \phi \, dx \quad \text{and} \quad l_f(\phi) = \int_\Omega f \phi \, dx, \tag{2.5}$$

respectively. For simplicity, we only consider non-homogeneous Dirichlet boundary conditions on $\partial\Omega$. However, the analysis presented in our paper can easily be generalized to other constellations of boundary conditions which ensure existence and uniqueness such as Robin or mixed boundary conditions.

Assumption 1. *We assume that the solution u of (2.4) belongs to $V = W^{1,2}(\Omega) \cap W^{l,2}(\mathcal{T}_H(\Omega))$ with some $l \geq 2$.*

Assumption 1 implies the following interface conditions, see [14],

$$[\![u]\!] = 0 \quad \text{on} \quad F, \quad \text{and} \quad [\![\rho \nabla u]\!] \cdot n_F = 0, \quad \text{on} \quad F, \tag{2.6}$$

where $[\![.]\!]|_F$ denotes the jumps on F, i.e., $[\![a]\!]|_F := a_1 - a_2$, and n_F is the unit normal vector on F.

In what follows, positive constants c and C appearing in inequalities are generic constants which do not depend on the mesh-size h. In many cases, we will indicate on what may the constants depend for an easier understanding of the proofs. Frequently, we will write $a \sim b$ meaning that $c\,a \leq b \leq C\,a$.

2.3. B-spline spaces

In this section, we briefly present the B-spline spaces and the form of the B-spline parametrizations for the physical subdomains. For a more detailed presentation we refer to [4], [5], [19].

Let us consider the unit cube $\widehat{\Omega} = (0,1)^d \subset \mathbb{R}^d$, which we will refer to as the parametric domain and let $\overline{\Omega} = \bigcup_{i=1}^N \overline{\Omega}_i$, with $\Omega_i \cap \Omega_j = \emptyset$, for $i \neq j$ be a decomposition of Ω. Let the integers k, $i = 1, ..., N$ and n_ι, $\iota = 1, ..., d$ denote the given B-spline degree, the corresponding physical $i-th$ subdomain, and the number of basis functions of the B-spline space that will be constructed in x_ι-direction. We introduce the $d-$dimensional vector of knots $\mathbf{\Xi}_i^d = (\Xi_i^1, ..., \Xi_i^\iota, ..., \Xi_i^d)$, $\iota = 1, \ldots, d$, with the particular components given by $\Xi_i^\iota = \{0 = \xi_1^\iota \leq \xi_2^\iota \leq ... \leq \xi_{n_\iota+k+1}^\iota = 1\}$. The components Ξ_i^ι of $\mathbf{\Xi}_i^d$ form a mesh $T_{h_i,\widehat{\Omega}}^{(i)} = \{\hat{E}_m\}_{m=1}^{M_i}$ in $\widehat{\Omega}$, where $\hat{E}_m$ are the micro elements and h_i is the mesh size, which is defined as follows. Given a micro element $\hat{E}_m \in T_{h_i,\widehat{\Omega}}^{(i)}$, we set $h_{\hat{E}_m} = diameter(\hat{E}_m) = \max_{x_1,x_2 \in \overline{\hat{E}}_m} \|x_1 - x_2\|_d$, where $\|.\|_d$ is the Euclidean norm in $\mathbb{R}^d$ and the subdomain mesh size h_i is defined to be $h_i = \max\{h_{\hat{E}_m}\}$. We define $h = \max_{i=1,...,N}\{h_i\}$.

Assumption 2. *The meshes* $T_{h_i,\widehat{\Omega}}^{(i)}$ *are quasi-uniform, i.e., there exist a constant* $\theta \geq 1$ *such that* $\theta^{-1} \leq h_{\hat{E}_m}/h_{\hat{E}_{m+1}} \leq \theta$. *Also, we assume that* $h_i \sim h_j$ *for* $i \neq j$.

Given the knot vector Ξ_i^ι in every direction $\iota = 1, ..., d$, we construct the associated univariate B-spline functions, $\hat{\mathbb{B}}_{\Xi_i^\iota,k} = \{\hat{B}_{1,\iota}^{(i)}(\hat{x}_\iota), ..., \hat{B}_{n_\iota,\iota}^{(i)}(\hat{x}_\iota)\}$ using the Cox-de Boor recursion formula, see details in [4], [5]. On the mesh $T_{h_i,\widehat{\Omega}}^{(i)}$, we define the multivariate B-spline space, $\hat{\mathbb{B}}_{\mathbf{\Xi}_i^d,k}$, to be the tensor-product of the corresponding univariate $\mathbb{B}_{\Xi_i^\iota,k}$ spaces. Accordingly, the B-spline functions of $\hat{\mathbb{B}}_{\mathbf{\Xi}_i^d,k}$ are defined by the tensor-product of the univariate B-spline basis functions, that is

$$\hat{\mathbb{B}}_{\mathbf{\Xi}_i^d,k} = \otimes_{\iota=1}^d \hat{\mathbb{B}}_{\Xi_i^\iota,k} = span\{\hat{B}_j^{(i)}(\hat{x})\}_{j=1}^{n=n_1\times...\times n_\iota\times...\times n_d}, \tag{2.7}$$

where each $\hat{B}_j^{(i)}(\hat{x})$ has the form

$$\hat{B}_j^{(i)}(\hat{x}) = \hat{B}_{j_1}^{(i)}(\hat{x}_1) \times ... \times \hat{B}_{j_\iota}^{(i)}(\hat{x}_\iota) \times ... \times \hat{B}_{j_d}^{(i)}(\hat{x}_d), \text{ with } \hat{B}_{j_\iota}^{(i)}(\hat{x}_\iota) \in \hat{\mathbb{B}}_{\Xi_i^\iota,k}. \tag{2.8}$$

Finally, having the B-spline spaces and the B-spline control points $C_j^{(i)}$, we can represent each subdomain Ω_i, $i = 1, ..., N$ by the parametric mapping

$$\mathbf{\Phi}_i : \widehat{\Omega} \rightarrow \Omega_i, \quad x = \mathbf{\Phi}_i(\hat{x}) = \sum_{j=1}^n C_j^{(i)} \hat{B}_j^{(i)}(\hat{x}) \in \Omega_i, \tag{2.9}$$

where $\hat{x} = \mathbf{\Psi}_i(x) := \mathbf{\Phi}_i^{-1}(x)$, cf. [4].

We construct a mesh $T_{h_i,\Omega_i}^{(i)} = \{E_m\}_{m=1}^{M_i}$ for every Ω_i, whose vertices are the images of the vertices of the corresponding parametric mesh $T_{h_i,\widehat{\Omega}}^{(i)}$ through $\mathbf{\Phi}_i$. For each $E \in T_{h_i,\Omega_i}^{(i)}$, we denote its support extension by $D_E^{(i)}$, where the support extension is defined to be the interior of the set formed by the union of the supports of all B-spline functions whose supports intersects E.

For $i = 1, ..., N$, we construct the B-spline space $\mathbb{B}_{\mathbf{\Xi}_i^d,k}$ on Ω_i by

$$\mathbb{B}_{\mathbf{\Xi}_i^d,k} := \{B_j^{(i)}|_{\Omega_i} : B_j^{(i)}(x) = \hat{B}_j^{(i)} \circ \mathbf{\Psi}_i(x), \text{ for } \hat{B}_j^{(i)} \in \hat{\mathbb{B}}_{\mathbf{\Xi}_i^d,k}\}. \tag{2.10}$$

The global B-spline space V_h with components on every $\mathbb{B}_{\mathbf{\Xi}_i^d,k}$ is defined by

$$V_h := V_{h_1} \times ... \times V_{h_N} := \mathbb{B}_{\mathbf{\Xi}_1^d,k} \times ... \times \mathbb{B}_{\mathbf{\Xi}_N^d,k}. \tag{2.11}$$

We refer the reader to [4] for more information about the meaning of the knot vectors in CAD and IgA.

Remark 2.1. *The B-spline spaces presented above are referred to the general case of* N *subdomains. In this paper, for the sake of simplicity, we assume that we have* $N = 2$. *The mappings in (2.9) produce (and are referred to) matching interface parametrizations. Throughout the paper it is understood that we study the case where the mappings in (2.9) produce non-matching interface parametrizations and a gap region appears between the adjacent subdomains, see Section 2.4.*

Assumption 3. *We assume that* $k \geq l$, *cf. Assumption 1.*

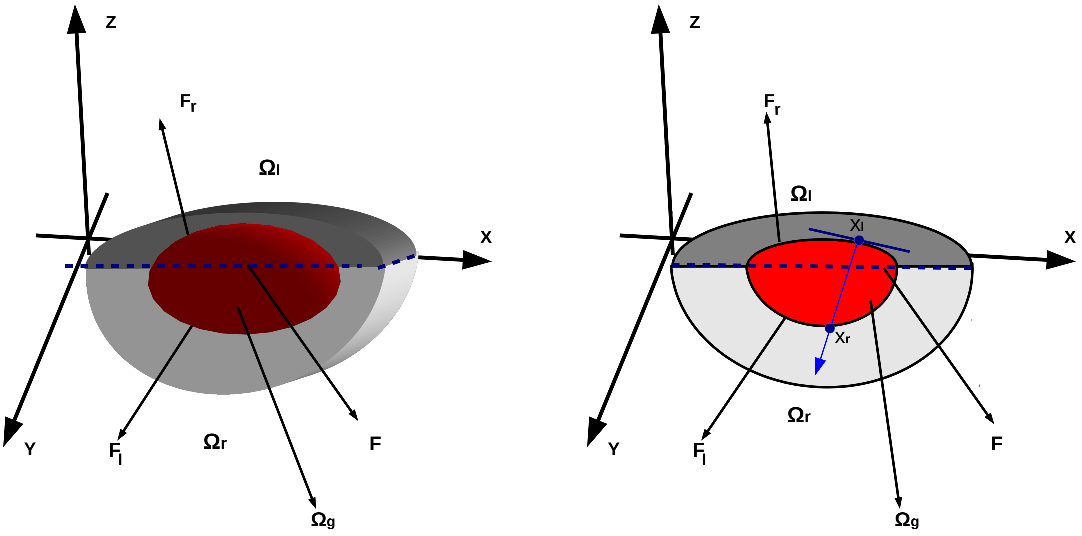

(a) (b)

Figure 1: (a) Illustration of the gap region (shown in red) between two adjacent sub domains in $d = 3$ case, (b) $2d$-view representation of the diametrically opposite points x_l and x_r located on $\partial\Omega_g$.

2.4. Non-matching interface parametrizations

In many realistic situations, it is necessary to perform a decomposition of the computational domain Ω into multiple subdomains (patches). Typical examples can be when different mathematical models are used in different parts of Ω or the case of complicated interface problems. It is convenient to consider the different parts as separate subdomains. In IgA framework, the subdomains are parametrized by using B-splines (NURBS, T-spline etc.) finite dimensional spaces, see [4]. In order to prepare the subdomain IgA parametrizations, we need firstly to define the corresponding control nets, see, e.g., [4], [9], [10], [15], [17]. We usually obtain compatible parametrizations for the common interfaces of the adjusting subdomains. The control points on a face are appropriately matched on the control points of the adjoining face, so as to obtain identical interface for the adjusting subdomains. For example, for the decomposition given in (2.1), the B-spline parametrizations of Ω_1 and Ω_2 must provide at the end an identical parametrization for the interface F. Despite the advantages, that B- splines (NURBS etc.) offer for the parametrization of the subdomains, some serious difficulties can arise, especially, when the subdomains topologically differ a lot from a cube. The segmentation procedure can lead us to incompatible parametrizations of the geometry, meaning that the parametrized interfaces of adjusting subdomains are not identical after the volume segmentation. We call this as a non-matching interface parametrization. The result of this phenomenon is the creation of overlapping subdomains or gap regions between adjacent subdomains. As in our previous work [8], so in this work, we study the later case. Here, we point out that the problem is considered in the case where the gap region will be maintained even after a local control net refinement procedure and the gap size can be expressed as a polynomial function of h.

2.5. The gap region

For simplicity, we consider the case where the decomposition includes only two subdomains and only one gap region appears between them. More precisely, we suppose that after a segmentation procedure, we obtain two B-spline control nets, which give incompatible parametrizations of the geometry of the subdomains Ω_1 and Ω_2 of (2.1). Thus, we have the parametrizations $\mathbf{\Phi}_l : \widehat{\Omega} \to \Omega_l$ and $\mathbf{\Phi}_r : \widehat{\Omega} \to \Omega_r$ correspondingly, which give non-matching interface parametrizations of F, and a gap region, say Ω_g, exists between Ω_l and Ω_r. As an immediate result we have that $\overline{\Omega} = \overline{\Omega}_l \cup \overline{\Omega}_g \cup \overline{\Omega}_r$, see an illustration in Fig. 1(a). In what follows, we will call Ω_l and Ω_r parametrized subdomains or simply subdomains, if there is no chance of confusion with Ω_i, $i=1,2$. We denote by $\mathcal{T}_H(\Omega\setminus\overline{\Omega}_g)=\{\Omega_l,\Omega_r\}$.

Without loss of generality, we suppose that $\partial\Omega_g=F_l\cup F_r$, see Fig. 1(b), and assume that there is a h_0 such that for all $h\leq h_0$ the following relations hold

$$F_l\subset\partial\Omega_l \quad \text{and} \quad F_r\subset\partial\Omega_r, \tag{2.12a}$$

$$\Omega_l\subseteq\Omega_1,\quad \Omega_r\subset\Omega_2,\quad \Omega_g\subset\Omega_1\cup\Omega_2,\quad \text{and}\quad \overline{\Omega}=\overline{\Omega}_l\cup\overline{\Omega}_g\cup\overline{\Omega}_r. \tag{2.12b}$$

The boundary face F_l is considered to be a simple region, and it can be described as the set of points (x,y,z) satisfying

$$0\leq x\leq x_M,\ \psi_1(x)\leq y\leq\psi_2(x),\ \phi_1(x,y)\leq z\leq\phi_2(x,y), \tag{2.13}$$

where x_M is a fixed real number, ψ_i and ϕ_i with $i=1,2$ are given continuous functions. An illustration is shown in Fig. 1(b). Our next goal is to assign the points $x_l\in F_l$ to the points of the other face $x_r\in F_r$, in order to build up later the numerical flux function. We follow the some ideas as in [8]. The assignment between the opposite points is achieved by constructing a one-to-one mapping $\mathbf{\Phi}_{l,r}:F_l\to F_r$. Let n_{F_l} be the unit normal vector on F_l and let n_{F_r} be the unit normal vector on F_r. Since only small gap regions are considered, we suppose that $n_{F_l}\approx -n_{F_r}$. Hence, we can define the mapping $\mathbf{\Phi}_{l,r}:F_l\to F_r$ as

$$\mathbf{\Phi}_{l,r}:x_l\in F_l\to\mathbf{\Phi}_{l,r}(x_l):=x_r\in F_r,\quad \text{with}\quad \mathbf{\Phi}_{l,r}(x_l)=x_l+\zeta_0(x_l)n_{F_l}, \tag{2.14}$$

where ζ_0 is a B-spline with $\|\zeta_0\|_{L^\infty}=1$. We define the corresponding mapping $\mathbf{\Phi}_{r,l}:F_r\to F_l$ to be

$$\mathbf{\Phi}_{r,l}(x_r)=(x_{l,1},x_{l,2},x_{l,3}),\ \text{where}\quad \mathbf{\Phi}_{l,r}(x_{l,1},x_{l,2},x_{l,3})=x_r. \tag{2.15}$$

We will see later that the parametrization mappings (2.15) and (2.14) simplify the analysis and are convenient for performing the numerical tests, see an extensively discussion for this in [8]. We mention that, in [8] the gap boundary face F_l is taken to belong in xy-plane and thus for the construction of the mapping $\mathbf{\Phi}_{l,r}$, see (2.14), the vector $n_{F_l}=(0,0,1)$ is utilized. The parametric mapping $\mathbf{\Phi}_{l,r}$ as defined in (2.14) generalize this case.

We finally characterize the points which belong in the interval $[x_l,x_r]$. To this end, for every $x_l\in F_l$ we construct a C^1 one-to-one map $\gamma_{x_l}:[0,1]\to\overline{\Omega}_g$,

$$\gamma_{x_l}(s)=x_l+s(x_r-x_l),\quad \text{with}\quad \mathbf{\Phi}_{l,r}(x_l)=x_r. \tag{2.16}$$

The function γ_{x_l} help us to quantify the size of the gap by introducing the gap distance defined by

$$d_g=\max_{x_l}\{|\gamma_{x_l}(0)-\gamma_{x_l}(1)|\}. \tag{2.17}$$

We focus on gap regions whose distance decreases polynomially in h, that is

$$d_g\leq h^\lambda,\quad \text{with}\quad \lambda\geq 1. \tag{2.18}$$

2.6. Jumps and dG norm $\|.\|_{dG}$

For the face F_i, $i=l,r$, let n_{F_i} be its unit normal vector towards Ω_g. For a smooth function ϕ defined on Ω, we define its interface averages and the jumps as

$$\begin{aligned}
[\![\phi]\!]|_{F_i}&=\Big(\phi_i-\phi_g\Big), & \{\phi\}|_{F_i}&=\frac{1}{2}\Big(\phi_i+\phi_g\Big),\\
[\![\rho\nabla\phi]\!]|_{F_i}\cdot n_{F_i}&=\Big(\rho_i\nabla\phi_i-\rho_g\nabla\phi_g\Big)\cdot n_{F_i}, & \{\rho\nabla\phi\}|_{F_i}\cdot n_{F_i}&=\frac{1}{2}\Big(\rho_i\nabla\phi_i+\rho_g\nabla\phi_g\Big)\cdot n_{F_i}.
\end{aligned} \tag{2.19}$$

To proceed to our analysis, we need to define the broken dG-norm, $\|.\|_{dG}$. For $v\in V+V_h$, we define

$$\|v\|_{dG}^2=\sum_{i=l,r}\Big(\rho_i\|\nabla v_i\|^2_{L^2(\Omega_i)}+\frac{\rho_i}{h}\|v_i\|^2_{L^2(\partial\Omega_i\cap\partial\Omega)}+\frac{\{\rho\}}{h}\|v_i\|^2_{L^2(F_i)}\Big). \tag{2.20}$$

3. The problem on $\Omega \setminus \overline{\Omega}_g$

Having B-spline spaces defined only on Ω_l and Ω_r, we need to derive a discrete problem in Ω_l and Ω_r and then to give as estimate for the error between u and the corresponding discrete solution u_h. The derivation of the problem on $\Omega \setminus \overline{\Omega}_g$ has been explained in [8]. For the completeness of the section, we repeat the main points and the final result.

Recall that $\overline{\Omega} = \overline{\Omega}_l \cup \overline{\Omega}_g \cup \overline{\Omega}_r$, see (2.12a). Now, multiplying (2.3) by a $\phi \in C_0^\infty(\Omega)$, integrating on every Ω_i separately, then performing integration by parts, summing over all subdomains, using the equality $[\![\rho\nabla u\phi]\!] = \{\rho\nabla u\}[\![\phi]\!] + [\![\rho\nabla u]\!]\{\phi\}$ and the interface conditions (2.6), we can show that the exact solution u of (2.4) satisfies

$$\begin{aligned}\int_{\Omega_l} \rho_l \nabla u \cdot \nabla\phi\, dx - \int_{\partial\Omega_l \cap \partial\Omega} \rho_l \nabla u \cdot n_{\partial\Omega_l} \phi\, d\sigma - \int_{F_l} \{\rho\nabla u\} \cdot n_{F_l} \phi\, d\sigma \\ + \int_{\Omega_r} \rho_r \nabla u \cdot \nabla\phi\, dx - \int_{\partial\Omega_r \cap \partial\Omega} \rho_r \nabla u \cdot n_{\partial\Omega_r} \phi\, d\sigma - \int_{F_r} \{\rho\nabla u\} \cdot n_{F_r} \phi\, d\sigma \\ = \int_{\Omega\setminus\overline{\Omega}_g} f\phi\, dx, \quad \text{for all} \quad \phi \in C_0^\infty(\Omega). \end{aligned} \tag{3.1}$$

For the consistency of (3.1) with the original problem (2.5), we refer to [8]. Looking at (3.1), we observe that the normal flux terms $\nabla u_g \cdot n_{\partial\Omega_g}$, e.g., $\int_{F_l} \{\rho\nabla u\} \cdot n_{F_l}\phi\, d\sigma = \int_{F_l} \frac{1}{2}(\rho_l \nabla u_l + \rho_g \nabla u_g) \cdot n_{F_l} \phi\, d\sigma$, are still unknown, in the sense that their values are not predefined for an explicit use in the computations. In order to get to the discrete analogue of (3.1), the normal flux terms $\nabla u_g \cdot n_{\partial\Omega_g}$ are approximated by Taylor expansions.

3.1. Approximations of normal fluxes $\nabla u_g \cdot n_{\partial\Omega_g}$.

We recall the following Taylor's formula with integral remainder, for $f \in C^m([0,1])$

$$f(1) = f(0) + \sum_{j=1}^{m-1} \frac{1}{j!} f^{(j)}(0) + \frac{1}{(m-1)!} \int_0^1 s^{m-1} f^{(m)}(1-s)\, ds. \tag{3.2}$$

Let us suppose for the moment that $u \in C^m(\Omega)$ with $m \geq 2$. Let $x_l = (x_{l,1}, x_{l,2}, x_{l,3})$ be a fixed point on F_l and let $x_r = \mathbf{\Phi}_{l,r}(x_l)$ be its corresponding diametrically opposite point on F_r. We apply Taylor expansions along the line γ_{x_l} (or γ_{x_r}), see (2.16), emanating from x_l (or x_r) and heading in the diametrically opposite point x_r (or x_l correspondingly). In that way, we produce approximations of $\rho_g \nabla u_g \cdot n_{\partial\Omega_g}|_{\partial\Omega_g}$ using u_l and u_r. Similar Taylor expansions have been used in [8] for approximating the fluxes $\rho_g \nabla u_g \cdot n_{\partial\Omega_g}|_{\partial\Omega_g}$ for simple gap shapes.

We define $f(s) = u(\gamma_{x_l}(s)) = u(x_l + s(x_r - x_l))$. By chain rule we can obtain

$$f^{(j)}(s) = \sum_{|\alpha|=j} \frac{j!}{\alpha!} D^\alpha u(x_l + s(x_r - x_l))(x_r - x_l)^\alpha, \tag{3.3}$$

where $\alpha! = \alpha_1!...\alpha_d!$ and $(x_r - x_l)^\alpha = (x_{r,1} - x_{l,1})^{\alpha_1}...(x_{r,d} - x_{l,d})^{\alpha_d}$. Combining (3.2) and (3.3), we obtain

$$u(x_r) = u(x_l) + \nabla u(x_l) \cdot (x_r - x_l) + R^2 u(x_r + s(x_l - x_r), \tag{3.4a}$$

where $R^2 u(x_r + s(x_l - x_r)$ is the $2-nd$ order remainder term defined by

$$R^2 u(x_r + s(x_l - x_r) = \sum_{|\alpha|=2} (x_r - x_l)^\alpha \frac{2}{\alpha!} \int_0^1 s D^\alpha u(x_r + s(x_l - x_r))\, ds. \tag{3.4b}$$

Now, we use (3.4) to approximate the flux terms $\nabla u_g \cdot n_{F_l}$ in (3.1). Denoting $r_l = x_r - x_l$ and $r_r = -r_l$, by (2.14) and (2.15), we conclude that $n_{F_l} = \frac{r_l}{|r_l|}$ and $n_{F_r} = \frac{r_r}{|r_r|}$. Using that $0 = [\![u]\!]|_{F_l} = (u_l(x_l) - u_g(x_l))$ and (3.4), we have

$$u_r(x_r) = u_g(x_l) + \nabla u_g(x_l) \cdot r_l + R^2 u_g(x_r + s(x_l - x_r) \tag{3.5a}$$

$$u_g(x_l) = u_r(x_r) - \nabla u_r(x_r) \cdot r_l + R^2 u_r(x_l + s(x_r - x_l), \tag{3.5b}$$

and we can obtain that

$$\nabla u_g \cdot n_{F_l} = \nabla u_r \cdot n_{F_l} - \frac{1}{|r_l|}\big(R^2 u_r(x_l + s(x_r - x_l)) + R^2 u_g(x_r + s(x_l - x_r))\big) \tag{3.6a}$$

$$-\frac{1}{h}\big(u_l(x_l) - u_r(x_r)\big) = \frac{|r_l|}{h}\nabla u_g(x_l) \cdot n_{F_l} + \frac{1}{h}R^2 u_g(x_r + s(x_l - x_r)). \tag{3.6b}$$

Following the same steps as in [8], we replace the normal fluxes on the boundary parts of $\partial\Omega_g$, by using the expressions (3.6). For $\phi_h \in V_h$, it follows by (3.6) that

$$\begin{aligned}
&\int_{F_l} \big(\frac{\rho_l}{2}\nabla u_l + \frac{\rho_g}{2}\nabla u_g\big) \cdot n_{F_l}\phi_h - \frac{\{\rho\}}{h}[\![u]\!]\phi_h \, d\sigma = \\
&\int_{F_l} \frac{\rho_l}{2}\nabla u_l \cdot n_{F_l}\phi_h + \frac{\rho_g}{2}\nabla u_r \cdot n_{F_l}\phi_h - \big(\frac{\rho_g}{2|r_l|}R^2 u_g(x_r + s(x_l - x_r)) + \frac{\rho_g}{2|r_l|}R^2 u_r(x_l + s(x_r - x_l))\big)\phi_h \\
&\qquad - \frac{\{\rho\}}{h}\big(u_l - u_r\big)\phi_h + \frac{\{\rho\}}{h}\big(|r_l|\nabla u_g \cdot n_{F_l} + R^2 u_g(x_r + s(x_l - x_r))\big)\phi_h \, d\sigma = \\
&\qquad\qquad \int_{F_l} \Big(\frac{\rho_l}{2}\nabla u_l + \frac{\rho_g}{2}\nabla u_r\Big) \cdot n_{F_l}\phi_h - \frac{\{\rho\}}{h}\big(u_l - u_r\big)\phi_h \, d\sigma - \\
&\qquad \int_{F_l} \Big(\frac{\rho_g}{2|r_l|}R^2 u_g(x_r + s(x_l - x_r)) + \frac{\rho_g}{2|r_l|}R^2 u_r(x_l + s(x_r - x_l))\Big)\phi_h \, d\sigma + \\
&\qquad\qquad\qquad \int_{F_l} \frac{\{\rho\}}{h}\Big(|r_l|\nabla u_g \cdot n_{F_l} + R^2 u_g(x_r + s(x_l - x_r))\Big)\phi_h \, d\sigma.
\end{aligned} \tag{3.7}$$

Now, using that $[\![\rho\nabla u]\!]|_{F_i} = 0$ for $i = l, r$, the assumption that $n_{F_l} \approx -n_{F_r}$, definition (2.15) and following the same procedure as above, we can derive the corresponding form for the flux term on F_r

$$\begin{aligned}
&\int_{F_r} \Big(\frac{\rho_r}{2}\nabla u_r + \frac{\rho_g}{2}\nabla u_g\Big) \cdot n_{F_r}\phi_h - \frac{\{\rho\}}{h}[\![u]\!]\phi_h \, d\sigma = \\
&\qquad\qquad \int_{F_r} \Big(\frac{\rho_r}{2}\nabla u_r + \frac{\rho_l}{2}\nabla u_l\Big) \cdot n_{F_r}\phi_h - \frac{\{\rho\}}{h}\big(u_r - u_l\big)\phi_h \, d\sigma - \\
&\qquad \int_{F_r} \Big(\frac{\rho_g}{2|r_r|}R^2 u_g(x_l + s(x_r - x_l)) + \frac{\rho_g}{2|r_r|}R^2 u_l(x_r + s(x_l - x_r))\Big)\phi_h \, d\sigma + \\
&\qquad\qquad\qquad \int_{F_r} \frac{\{\rho\}}{h}\Big(|r_r|\nabla u_g \cdot n_{F_r} + R^2 u_g(x_l + s(x_r - x_l))\Big)\phi_h \, d\sigma.
\end{aligned} \tag{3.8}$$

3.2. The dG IgA problem on $\Omega \setminus \overline{\Omega}_g$

For convenience we adopt the notations $R^2u_g(x_l) := R^2u_g(x_r + s(x_l - x_r))$, $R^2u_r(x_r) := R^2u_r(x_l + s(x_r - x_l))$ and $R_{\nabla,i} = \{\rho\}\big(\frac{|r_i|}{h}\nabla u_g \cdot n_{F_i} + \frac{1}{h}R^2u_g(x_i)\big)$, for $i = l, r$. Recalling (3.1) and utilizing the flux approximations (3.7) and (3.8), we deduce that the exact solution u satisfies

$$\begin{aligned}
&\int_{\Omega_l} \rho_l\nabla u \cdot \nabla\phi_h \, dx - \int_{\partial\Omega_l\cap\partial\Omega} \rho_l\nabla u \cdot n_{\partial\Omega_l}\phi_h \, d\sigma \\
&\qquad\qquad - \int_{F_l} \Big(\frac{\rho_l}{2}\nabla u_l + \frac{\rho_r}{2}\nabla u_r\Big) \cdot n_{F_l}\phi_h - \frac{\{\rho\}}{h}\big(u_l - u_r\big)\phi_h \, d\sigma \\
&\qquad\qquad + \int_{F_l} \Big\{R_{\nabla,l} + \frac{\rho_g}{2|r_l|}R^2u_r(x_r) + \frac{\rho_g}{2|r_l|}R^2u_g(x_l)\Big\}\phi_h \, d\sigma \\
&\qquad + \int_{\Omega_r} \rho_r\nabla u \cdot \nabla\phi_h \, dx - \int_{\partial\Omega_r\cap\partial\Omega} \rho_r\nabla u \cdot n_{\partial\Omega_r}\phi_h \, d\sigma \\
&\qquad\qquad - \int_{F_r} \Big(\frac{\rho_r}{2}\nabla u_r + \frac{\rho_l}{2}\nabla u_l\Big) \cdot n_{F_r}\phi_h - \frac{\{\rho\}}{h}\big(u_r - u_l\big)\phi_h \, d\sigma \\
&\qquad + \int_{F_r} \Big\{R_{\nabla,r} + \frac{\rho_g}{2|r_r|}R^2u_l(x_l) + \frac{\rho_g}{2|r_r|}R^2u_g(x_r)\Big\}\phi_h \, d\sigma = \int_{\Omega\setminus\overline{\Omega}_g} f\phi_h \, dx, \text{ for } \phi_h \in V_h,
\end{aligned} \tag{3.9}$$

We observe that the terms appearing in (3.9) are the terms that are expected to be appear in a dG scheme, of course, excluding the Taylor remainder terms. In view of this, we define the forms $B_{\setminus\Omega_g}(\cdot,\cdot)$:

$(V+V_h)\times V_h \to \mathbb{R}$, $R^2_{F_l}(\cdot,\cdot) : (V+V_h)\times V_h \to \mathbb{R}$, $R^2_{F_r}(\cdot,\cdot) : (V+V_h)\times V_h \to \mathbb{R}$, $R_{\Omega_g}(\cdot,\cdot) : (V+V_h)\times V_h \to \mathbb{R}$ and the linear functional $l_{f,\setminus\Omega_g} : V_h \to \mathbb{R}$ by

$$\begin{aligned} B_{\setminus\Omega_g}(u,\phi_h) = &\int_{\Omega_l} \rho_l \nabla u\cdot\nabla\phi_h\,dx - \int_{\partial\Omega_l\cap\partial\Omega} \rho_l\nabla u\cdot n_{\partial\Omega_l}\phi_h\,d\sigma \\ &- \int_{F_l}\Big(\frac{\rho_l}{2}\nabla u_l + \frac{\rho_r}{2}\nabla u_r\Big)\cdot n_{F_l}\phi_h - \frac{\{\rho\}}{h}(u_l-u_r)\phi_h\,d\sigma \\ &+ \int_{\Omega_r} \rho_r\nabla u\cdot\nabla\phi_h\,dx - \int_{\partial\Omega_r\cap\partial\Omega}\rho_r\nabla u\cdot n_{\partial\Omega_r}\phi_h\,d\sigma \\ - &\int_{F_r}\Big(\frac{\rho_r}{2}\nabla u_r + \frac{\rho_l}{2}\nabla u_l\Big)\cdot n_{F_r}\phi_h - \frac{\{\rho\}}{h}(u_r-u_l)\phi_h\,d\sigma, \end{aligned} \tag{3.10a}$$

$$R^2_{F_l}(u,\phi_h) = \int_{F_l}\Big\{\frac{\rho_g}{2|r_l|}R^2u_r(x_r)\phi_h + \frac{\rho_g}{2|r_l|}R^2u_g(x_l)\phi_h\Big\}\,d\sigma \tag{3.10b}$$

$$R^2_{F_r}(u,\phi_h) = \int_{F_r}\Big\{\frac{\rho_g}{2|r_r|}R^2u_l(x_l)\phi_h + \frac{\rho_g}{2|r_r|}R^2u_g(x_r)\phi_h\Big\}\,d\sigma, \tag{3.10c}$$

$$\begin{aligned} R_{\Omega_g}(u,\phi_h) = &\int_{F_l}\Big\{R_{\nabla,l}\phi_h + \frac{\rho_g}{2|r_l|}R^2u_r(x_r)\phi_h + \frac{\rho_g}{2|r_l|}R^2u_g(x_l)\phi_h\Big\}\,d\sigma \\ &+ \int_{F_r}\Big\{R_{\nabla,r}\phi_h + \frac{\rho_g}{2|r_r|}R^2u_l(x_l)\phi_h + \frac{\rho_g}{2|r_r|}R^2u_g(x_r)\phi_h\Big\}\,d\sigma, \end{aligned} \tag{3.10d}$$

$$l_{f,\setminus\Omega_g}(\phi_h) = \int_{\Omega\setminus\overline{\Omega}_g} f\phi_h\,dx. \tag{3.10e}$$

We note that the forms $R^2_{F_l}$ and $R^2_{F_r}$ appear in (3.10) have not been introduced in [8] for the derivation of the dG IgA scheme in case of simple gap regions. For the case under consideration, the introduction of $R^2_{F_l}$ and $R^2_{F_r}$ simplifies the analysis of the method. For establishing the dG IgA discrete problem, we prefer the absence of the terms related to Taylor residuals in the discrete form. Also, we wish the weak enforcement of the Dirichlet boundary conditions. We define the dG IgA scheme following the same procedure as in [8]. We introduce the bilinear form $B_h(\cdot,\cdot) : V_h\times V_h \to \mathbb{R}$ and the linear form $F_h : V_h \to \mathbb{R}$ as follows

$$B_h(u_h,\phi_h) = B_{\setminus\Omega_g}(u_h,\phi_h) + \sum_{i=l,r}\frac{\rho_i}{h}\int_{\partial\Omega_i\cap\partial\Omega} u_h\phi_h\,d\sigma, \tag{3.11}$$

$$F_h(\phi_h) = l_{f,\setminus\Omega_g}(\phi_h) + \sum_{i=l,r}\frac{\rho_i}{h}\int_{\partial\Omega_i\cap\partial\Omega} u_D\phi_h\,d\sigma. \tag{3.12}$$

Finally, the discrete problem is: find $u_h \in V_h$ such that

$$B_h(u_h,\phi_h) = F_h(\phi_h), \quad \text{for all } \phi_h \in V_h. \tag{3.13}$$

An immediate result is that, for the exact solution $u \in V$, the variational identity

$$B(u,\phi_h) := B_h(u,\phi_h) + R_{\Omega_g}(u,\phi_h) = F_h(\phi_h),\ \forall\phi \in V_h, \tag{3.14}$$

holds. Next we show several results that are going to be used in the error analysis.

Lemma 3.1. *Under the Assumption 2 and relation (2.18), there exist positive constants* $C_1(\rho,d)$ *and* $C_2(\rho,d)$ *such that the estimate*

$$|R_{\Omega_g}(u,\phi_h)| \le C_1\|\phi_h\|_{dG}\big(\|\nabla u_g\|_{L^2(\partial\Omega_g)} + \|\kappa_2\|_{L^2(\Omega_g)}\big)h^\beta, \tag{3.15a}$$

$$|R^2_{F_i}(u,\phi_h)| \le C_2\|\phi_h\|_{dG}\|\kappa_2\|_{L^2(\Omega_g)}h^\gamma, \quad i=1,2, \tag{3.15b}$$

holds true for all $(u,\phi_h) \in V\times V_h$, *where* $\kappa_2 = \big(\sum_{|\alpha|=2}|D^\alpha u|\big)$, $\beta = \lambda - \frac{1}{2}$, *and* $\gamma = \lambda + 1$.

Proof. Estimate (3.15a) results directly from Lemma 6 in [8].
Estimate (3.15b) follows easily from the estimate given in Lemma 5 in [8] by setting $p = 2$. □

Lemma 3.2. *Let* $\beta = \lambda - \frac{1}{2}$ *and* $\gamma = \lambda + 1$. *Then there is a constant* $C = C(\rho) \ge 0$ *independent of* h *such that the estimate*

$$B_h(u,\phi_h) \le C(\rho)\Big(\big(\|u\|^2_{dG} + \sum_{i=l,r}h\|\nabla u_i\|^2_{L^2(\partial\Omega_i)}\big)^{\frac{1}{2}} + \mathcal{K}_2(h^\gamma + h^\beta)\Big)\|\phi_h\|_{dG}, \tag{3.16}$$

holds for all $(u,\phi_h) \in (V+V_h)\times V_h$, *where* $\mathcal{K}_2 = \|\nabla u_g\|_{L^2(\partial\Omega_g)} + \|\kappa_2\|_{L^2(\Omega_g)}$.

Proof. By an application of CauchySchwarz inequality, we can show

$$\Big|\sum_{i=l,r}\int_{\Omega_i}\rho_i^{\frac{1}{2}}\nabla u\cdot\rho_i^{\frac{1}{2}}\nabla\phi_h\,dx\Big|\leq\|u\|_{dG}\|\phi_h\|_{dG}. \tag{3.17}$$

Next, we give bounds for the normal flux terms on $\partial\Omega_l$. A direct application of Lemma 5.2 in [13] gives

$$\Big|\int_{\partial\Omega_l\cap\partial\Omega}\rho_l\nabla u\cdot n_{\partial\Omega_l}\phi_h\,d\sigma\Big|\leq C\Big(h\|\nabla u_l\|^2_{L^2(\partial\Omega_l\cap\partial\Omega)}\Big)^{\frac{1}{2}}\|\phi_h\|_{dG}. \tag{3.18}$$

For the flux terms on F_l, the triangle inequality and relations (2.6) and (3.6a) yield

$$\begin{aligned}\Big|\int_{F_l}\Big(\frac{\rho_l}{2}\nabla u_l+\frac{\rho_r}{2}\nabla u_r\Big)\cdot n_{F_l}\phi_h\,d\sigma\Big| &\leq\Big|\int_{F_l}\rho_l\nabla u_l\cdot n_{F_l}\phi_h\,d\sigma\Big|+\Big|\int_{F_l}\rho_r\nabla u_r\cdot n_{F_l}\phi_h\,d\sigma\Big|\\ &\leq\Big|\int_{F_l}\rho_l\nabla u_l\cdot n_{F_l}\phi_h\,d\sigma\Big|+\Big|\int_{F_l}\Big(\rho_r\nabla u_g\cdot n_{F_l}+\frac{\rho_r}{|r_l|}\big(R^2u_r(x_r)+R^2u_g(x_l)\big)\Big)\phi_h\,d\sigma\Big|\\ &\leq C(\rho)\Big|\int_{F_l}\nabla u_l\cdot n_{F_l}\phi_h\,d\sigma\Big|+C(\rho)\Big|\int_{F_l}\frac{1}{|r_l|}\big(R^2u_r(x_r)+R^2u_g(x_l)\big)\phi_h\,d\sigma\Big|\\ &\leq C(\rho)\Big(h\|\nabla u_l\|^2_{L^2(F_l)}\Big)^{\frac{1}{2}}\|\phi_h\|_{dG}+C(\rho)\|\phi_h\|_{dG}\|\kappa_2\|_{L^2(\Omega_g)}h^{\gamma},\end{aligned} \tag{3.19}$$

where the estimate (3.15b) has been used. The flux terms of $B_h(\cdot,\cdot)$, which appear on F_r can be bound in a similar way. As a last step, we need to bound the jump terms in $B_h(\cdot,\cdot)$. Following similar procedure as in (3.19) and using (3.6b) and estimate (3.15a), we can show

$$\Big|\int_{F_l}\frac{\{\rho\}}{h}\big(u_l-u_r\big)\phi_h\,d\sigma\Big|\leq\Big|C(\rho)\int_{F_l}\Big(\frac{|r_l|}{h}\nabla u_g(x_l)\cdot n_{F_l}+\frac{1}{h}R^2u_g(x_l)\Big)\phi_h\,d\sigma\Big| \tag{3.20}$$

$$\leq C(\rho)\|\phi_h\|_{dG}\big(\|\nabla u_g\|_{L^p(\partial\Omega_g)}+\|\kappa_2\|_{L^p(\Omega_g)}\big)h^{\beta}. \tag{3.21}$$

Working in similar way, we can show

$$\Big|\int_{F_r}\frac{\{\rho\}}{h}\big(u_r-u_l\big)\phi_h\,d\sigma\Big|\leq C(\rho)\|\phi_h\|_{dG}\big(\|\nabla u_g\|_{L^p(\partial\Omega_g)}+\|\kappa_2\|_{L^p(\Omega_g)}\big)h^{\beta}. \tag{3.22}$$

Finally, collecting all the above bounds we can deduce assertion (3.16). □

We point out that the terms $\mathcal{K}_2(h^{\gamma}+h^{\beta})$ in (3.16) appear due to the estimation of the multi-directional Taylor remainder terms, which are involved in the approximation of the normal fluxes in $\partial\Omega_g$. In [8], we follow a different idea for showing the corresponding boundedness property for $B_h(.,.)$. This idea is convenient for the uni-axial Taylor expansions and we avoid the appearance of the terms $\mathcal{K}_2(h^{\gamma}+h^{\beta})$ in the boundedness property of $B_h(.,.)$.

Now, we prove that the discrete problem (3.13) has unique solution.

Lemma 3.3. *The bilinear form $B_h(\cdot,\cdot)$ in (3.11) is bounded and elliptic on V_h, i.e., there are positive constants C_M and C_m such that the estimates*

$$B_h(v_h,\phi_h)\leq C_M\|v_h\|_{dG}\|\phi_h\|_{dG}\quad\textit{and}\quad B_h(v_h,v_h)\geq C_m\|v_h\|^2_{dG}, \tag{3.23}$$

hold for all $\phi_h\in V_h$.

Proof. The two properties of $B_h(\cdot,\cdot)$ can be shown following the same procedure as in Lemma 3.2 and mimic the proofs of Lemma 4.5 and Lemma 4.6 in [13]. Thus, the details are omitted. □

Since $B_h(.,.)$ is bounded and elliptic in V_h, we can apply the Lax-Milgram theorem to conclude that the problem (3.13) has a unique solution. Note that the solution u satisfies (3.14) but does not satisfy the discrete problem (3.13). The derived dG IgA discretization is not consistent. We present below the error analysis borrowing ideas from the weak consistent FE methods, [6].

4. Error estimates

Next, we derive error estimate for the proposed dG IgA scheme (3.13) under the Assumption 1. The procedure that we follow is similar to the corresponding procedure followed in [8]. The main differences are due to the different bound estimate (3.16). For the completeness of the paper, we present the error analysis and we highlight the dependence of the analysis on the bound estimate (3.16). The linearity of the $B_h(\cdot,\cdot)$, see (3.11) and (3.10), and the relations (3.12) and (3.14) yield

$$\begin{aligned} B_h(u_h - z_h, \phi_h) &= B(u, \phi_h) + \sum_{i=l,r} \frac{\rho_i}{h} \int_{\partial\Omega_i \cap \partial\Omega} (u - u_D)\phi_h \, d\sigma - B_h(z_h, \phi_h) + F_h(\phi_h) - l_{f,\setminus\overline{\Omega}_g}(\phi_h) \\ &= B_h(u, \phi_h) + R_{\Omega_g}(u, \phi_h) - \sum_{i=l,r} \frac{\rho_i}{h} \int_{\partial\Omega_i \cap \partial\Omega} u_D\phi_h \, d\sigma - B_h(z_h, \phi_h) + \sum_{i=l,r} \frac{\rho_i}{h} \int_{\partial\Omega_i \cap \partial\Omega} u_D\phi_h \, d\sigma \\ &= B_h(u - z_h, \phi_h) + R_{\Omega_g}(u, \phi_h). \end{aligned} \tag{4.1}$$

We choose in (4.1) $\phi_h = u_h - z_h$. Let $\mathcal{K}_2 = \|\nabla u_g\|_{L^2(\partial\Omega_g)} + \|\kappa_2\|_{L^2(\Omega_g)}$ and the parameters $\beta = \lambda - \frac{1}{2}$, and $\gamma = \lambda + 1$. Then, Lemma 3.3 and Lemma 3.2 imply

$$\begin{aligned} C_m\|u_h - z_h\|_{dG}^2 &\leq C_M\Big(\big(\|u - z_h\|_{dG}^2 + \sum_{i=l,r} h\|\nabla(u - z_h)\|_{L^2(\partial\Omega_i)}^2\big)^{\frac{1}{2}} + \mathcal{K}_2\big(h^\beta + h^\gamma\big)\Big)\|u_h - z_h\|_{dG} + |R_{\Omega_g}(u, u_h - z_h)| \\ &\leq C_M\big(\|u - z_h\|_{dG}^2 + \sum_{i=l,r} h\|\nabla(u - z_h)\|_{L^2(\partial\Omega_i)}^2\big)^{\frac{1}{2}}\|u_h - z_h\|_{dG} + C_1\|u_h - z_h\|_{dG}(h^\beta + h^\gamma)\mathcal{K}_2, \end{aligned} \tag{4.2}$$

where we previously used the estimates (3.15) and (3.16). Applying triangle inequality in (4.2), we can easily arrive at the following estimate

$$\|u - u_h\|_{dG} \leq C\Big(\big(\|u - z_h\|_{dG}^2 + \sum_{i=l,r} h\|\nabla(u - z_h)\|_{L^2(\partial\Omega_i)}^2\big)^{\frac{1}{2}} + (h^\beta + h^\gamma)\,\mathcal{K}_2\Big), \tag{4.3}$$

where the constant C is specified by the constants appearing in (4.2). Now, we can prove the main error estimate.

Theorem 4.1. *Let u be the solution of problem (3.14), u_h be the corresponding dG IgA solution of problem (3.13), and let $d_g = h^\lambda$ with $\lambda \geq 1$. Then the error estimate*

$$\|u - u_h\|_{dG} \lesssim h^r\big(\sum_{i=l,r} \|u\|_{W^{l,2}(\Omega_i)} + \mathcal{K}_2\big), \tag{4.4}$$

holds, where $r = \min(s, \beta)$ with $s = \min(k+1, l) - 1$ and $\beta = \lambda - \frac{1}{2}$, and as usual $\mathcal{K}_2 = \|\nabla u_g\|_{L^2(\partial\Omega_g)} + \|\kappa_2\|_{L^2(\Omega_g)}$ with $\kappa_2 = \big(\sum_{|\alpha|=2} |D^\alpha u|\big)$.

Proof. The required estimate follows easily by applying in (4.3) the quasi-interpolation estimates given in [13] and then following the same steps as in Theorem 1 in [8]. □

5. Numerical tests

In this section, we perform several numerical tests with different gap shape and investigate the order of accuracy of the dG IgA scheme proposed in (3.11). We discuss two-, three- and four-dimensional test examples. All examples have been performed using second order ($k = 2$) B-spline spaces, apart from one where third order ($k = 3$) B-splines have been used. We compare the error convergence rates vs the grid size for several gap distances $d_g = h^\lambda$, with $\lambda = 1$, $\lambda = 2$, $\lambda = 3$ and $\lambda = 4$. Every example has been solved applying several mesh refinement steps with $h_i, h_{i+1}, ...$, satisfying Assumption 2. The numerical convergence rates r have been computed by the ratio $r = \frac{ln(e_i/e_{i+1})}{ln(h_i/h_{i+1})}$, $i = 1, 2, ...$, where the error $e_i := \|u - u_h\|_{dG}$ is always computed on the meshes $T^{(l)}_{h_i,\Omega_l} \cup T^{(r)}_{h_i,\Omega_r}$. We mention that, in the test cases we use highly smooth solutions, i.e., $k + 1 \leq l$, and therefore the parameter s in the approximation order in (4.4) becomes $s = k$. The predicted values of power β, the order s and the order r in (4.4) for several values of λ are displayed in Table 1. All tests have been performed in G+SMO[1], which is a generic object-oriented C++ library for IgA computations, see also [11, 12].

---

[1] G+SMO: https://www.gs.jku.at/trac/gismo

	B-spline degree k			
	Smooth solutions, $u \in W^{l \geq k+1, p=2}$			
$d_g = h^{\lambda}$	$\lambda = 1$	$\lambda = 2$	$\lambda = 3$	$\lambda = 4$
$\beta :=$	0.5	1.5	2.5	3.5
$s :=$	k	k	k	k
$r :=$	0.5	1.5	$\min(k, \beta)$	k

Table 1: The values of the predicted order r of the estimate (4.4) in Theorem 1.

For the two dimensional examples, we use the knot vectors $\Xi_i^1 = \{0, 0, 0, 0.5, 0.5, 1, 1, 1\}$ and $\Xi_i^2 := \{0, 0, 0, 0.5, 1, 1, 1\}$, with $i = 1, 2$, to define the parametric mesh and to construct the corresponding second order B-spline space, see (2.7). The B-spline parametrizations of Ω_1 and Ω_2, see (2.9), are constructed using the control points which are presented in the first two rows in Table 2. In any test case, the gap region is artificially created by moving the control points, which are related to the interface F, in the direction of n_F or of $-n_F$.

The numerical examples presented in [8] have been performed by using matching mesh conditions on F_l and F_r, without this to be restricted by the developing of the dG IgA method. In general, the introduction of dG techniques on the subdomain interfaces makes easier the use of non-matching meshes, see [13]. The proposed dG IgA method in Subsection 3.2 allows the use of non-matching meshes on the opposite gap boundaries. Keeping a constant linear relation between the sizes of the different meshes the approximation properties of the method are not affected, see [13]. In the Example 3 below, we exploit this advantage of the dG methods and solve the problem considering non-matching meshes on F_l and F_r. The convergence rates expected to be the same as those displayed in Table 1.

Control points C_{j_1,j_2} for Ω_1	(-6.5,-1.5), (-7,-1.5), (-7.5,-1.5), (-8,-1.5), (-8.5,-1.5), (-6.5,-0.5), (-7,0), (-7.5,0.25), (-8,0.5), (-8.5,0.5), (-5.5,0), (-5.5,1.25), (-5.5,2.125), (-5.5,3), (-5.5,3.5), (0,0) (-1.25,1.25), (-2.125,2.125), (-3,3), (-3.5,3.5)
Control points C_{j_1,j_2} for Ω_2	(6.5,-1.5), (-7,-1.5), (7.5,-1.5), (8,-1.5), (8.5,-1.5), (6.5,-0.5), (7,0), (7.5,0.25), (8,0.5), (8.5,0.5), (5.5,0), (5.5,1.25), (5.5,2.125), (5.5,3), (5.5,3.5), (0,0), (-1.25,1.25), (-2.125,2.125), (-3,3), (-3.5,3.5)
Control points C_{j_1,j_2} for Ω_r	(6.5,-1,5), (7,1.5), (7.5,-1,5), (8,-1.5), (8.5,-1.5), (6.5,-0.5),(7,0), (7.5,0.25), (8,0.5), (8.5,0.5), (5.5,0), (5.5,1.25), (5.5,2.125), (5.5,3), (5.5,3.5), (0,0), (0.25,2.75), (-0.625,3.625), (-1.5,4.5), (-3.5,3.5)

Table 2: The control points for the B-spline parametrizations of the subdomains

5.1. Two-dimensional numerical examples

Example 1, uniform diffusion coefficient $\rho_l = \rho_r$. The first numerical example is a simple test case demonstrating the applicability of the proposed technique for constructing dG IgA scheme on subdivisions including gaps with general shape. The domain Ω with the subdomains Ω_1, Ω_2 and the control net are shown in Fig. 2(a). The interface F, see (2.1), is given by $F = \{(x, y) : y = -x, \ -3.5 \leq x \leq 0\}$, see Fig. 2(a). The Dirichlet boundary condition and the right hand side f are determined by the exact solution $u(x, y) = \sin(\pi(x + 0.4)/6)\sin(\pi(y + 0.3)/3) + x + y$. In this example, we consider the homogeneous diffusion case, i.e., $\rho_l = \rho_r = 1$. In Fig. 2(b), we can see the initial subdomains Ω_l, Ω_r, and the gap region Ω_g in case $d_g = h^{\lambda=1}$. For this example the interface F coincides with F_l, the subdomain Ω_l coincides with Ω_1 and the corresponding control points of Ω_r are given in the last row in Table 2.

We performed three computations, where for every computation, the size of d_g was defined to be $\mathcal{O}(h^{\lambda})$, with $\lambda = 1, 2$ and 3. The numerical convergence rates for several levels of mesh refinement are plotted in Fig. 2(c). They are in good agreement with the theoretically predicted estimates given in Theorem 4.1. In particular for the case $d_g = h$, the rates are $r = 0.5$, and for the case $d_g = h^2$ the rates are $r = 1.5$, as it was expected, see Table 1. For the case of $d_g = h^3$, the rates related to the first refinements are little higher than the expected rates, but progressively tend to get the optimal value $r = 2$, see Table 1.

Example 2, different diffusion coefficient $\rho_l \neq \rho_r$. In the second example, we study the case of having smooth solutions on Ω_1 and Ω_2 but discontinuous coefficient, i.e., we set $\rho_1 = 1$ in Ω_1 and $\rho_2 = 3$ in Ω_2. The domain Ω and the subdomains Ω_1 and Ω_2 are presented in Fig. 2(a). The interface is

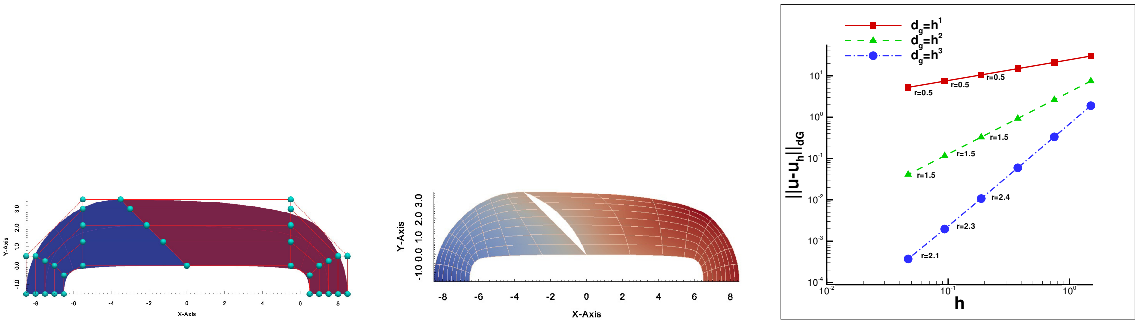

(a) (b) (c)

Figure 2: Example 1: (a) The subdomains Ω_1, Ω_2 with the corresponding control nets. (b) The contours of the u_h solution for $d_g = h$. (c)) The convergence rates for $d_g = \mathcal{O}(h^{\lambda})$ with $\lambda = 1, 2$ and 3.

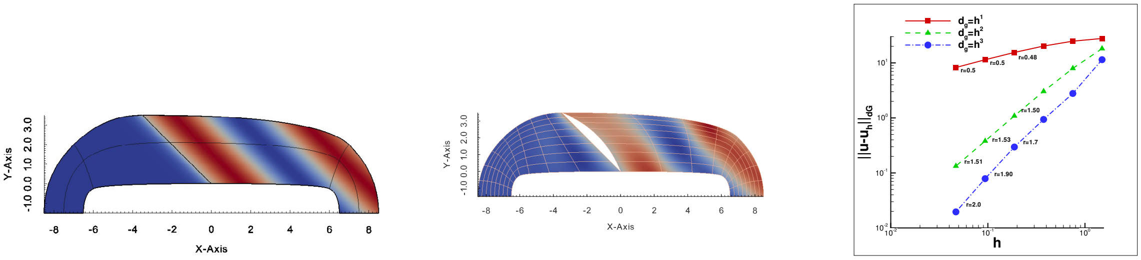

(a) (b) (c)

Figure 3: Example 2: (a) The contours of exact u given by (5.1), (b) The contours of u_h on subdomains Ω_l, Ω_r , (c) The convergence rates for the three choices of λ.

$F = \{(x, y) : y = -x, \ -3.5 \leq x \leq 0\}$, and the gap has the same shape as in Example 1, see Fig. 2(b). The exact solution is given by the formula

$$u(x, y) = \begin{cases} \exp(3(x + y)) - 1 & \text{if } (x, y) \in \Omega_1, \\ \sin(x + y) & \text{if } (x, y) \in \Omega_2. \end{cases} \tag{5.1}$$

The boundary conditions and the source function f are determined by (5.1). Note that in this test case, we have $[\![u]\!]|_F = 0$ as well $[\![\rho \nabla u]\!]|_F \cdot n_F = 0$ for the normal flux on F. The contours of the exact solution on the domain Ω are presented in Fig. 3(a). The problem has been solved on meshes refined following a sequential process, where we set $d_g = h^{\lambda}$, with $\lambda = 1, 2$ and 3. Thus for every computation the gap boundary is formed by the choice of h and λ. In Fig. 3(b), we plot the u_h solution on $\overline{\Omega} \setminus \Omega_g$ computed on the first initial mesh with $h = 0.5$. The computed rates are presented in Fig. 3(c). For the cases where $\lambda = 1$ and $\lambda = 2$, we observe that the values of the rates behave according to the predicted rates, see (4.4) and Table 1. The error corresponding to the $d_g = h^3$ test case (dashed dot line) on the first refinements appears to decay slower than it was expected, but finally on the last refinement levels tends to take the optimal value, which has predicted by the theory. By this example we validate numerically the predicted convergence rates for problems with discontinuous coefficient and smooth solutions.

Example 3, non-matching meshes. In the third test case, we apply the proposed method (3.11), in case of having a more complex gap region. Again the domain Ω is the same as in the previous examples, see Fig. 2(a) and the interface F is given by $F = \{(x, y) : y = -x, \ -3.5 \leq x \leq 0\}$. Here, we artificially created the gap region such that $\Omega_1 \cap \Omega_g \neq \emptyset$ and thus $F_l \neq F$. The shape of the gap region can be seen in Fig. 4(a). Note that the normal vector n_{F_l} is not fixed as in the previous examples. The exact solution of the problem is

$$u(x, y) = \begin{cases} \exp(\sin(x + y)) - 1 & \text{if } (x, y) \in \Omega_1, \\ \sin(2(x + y)) & \text{if } (x, y) \in \Omega_2. \end{cases} \tag{5.2}$$

The source function f and u_D are manufactured by the exact solution. The diffusion coefficient has been defined to be $\rho_1 = 2$ and $\rho_2 = 1$ and it holds $[\![u]\!]|_F \cdot n_F = 0$ as well $[\![\rho \nabla u]\!]|_F = 0$ for the normal flux

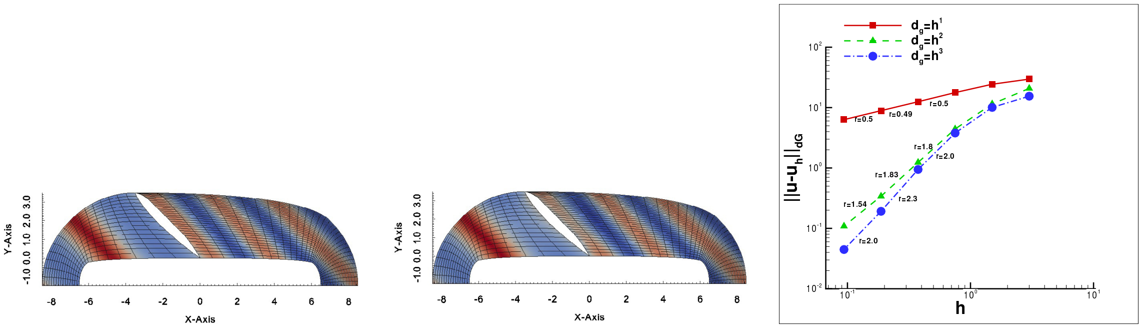

(a) (b) (c)

Figure 4: Example 3, non-matching meshes: (a) The contours of u on Ω_l and Ω_r with $d_g = 0.1875$. (b) The contours of u_h on Ω_l and Ω_r computed for $d_g = 0.1875$ (c) Convergence rates r for the three values of λ.

on F. The purpose of this example is the following: we want to investigate the convergence rates of the method by solving the problem in case of complex gap regions using non-matching meshes on F_l and F_r. In particular the relation between the mesh size h_l of Ω_l and the mesh size h_r of Ω_r is $h_l = 2h_r$.

Hence, for validation, we have computed the convergence rates of varying size $d_g = h_r^\lambda$ for $\lambda = 1$, $\lambda = 2$ and $\lambda = 3$. In Fig. 4(a), we plot the contours of u on the domains Ω_l and Ω_r on different meshes in case of $d_g = 0.1875$. In Fig. 4(b), we can see the contours of u_h, which has been computed using the different meshes. In Fig. 4(c), we plot the convergence rates for $\lambda = 1$, 2 and 3. We observe that the values of the rates for all three different λ cases confirm the theoretically predicted rates, see Table 1. The computational rates get the optimal value $r = 2$ for $\lambda = 3$, which is in agreement with the previous examples and is the expected value for this problem with smooth solution.

By this example, we demonstrated the ability of the proposed method to approximate oscillatory solutions of the diffusion problem (2.5) with the expected accuracy, in case of complex gab regions using different subdomain meshes.

Example 4, third order B-spline solutions. For this example, we again consider the problem (2.4) on the same domain Ω presented in Fig. 2(a), which is decomposed into the same subdomains Ω_1, Ω_2 and the common interface F as in the previous examples. The exact solution is now defined by

$$u(x,y) = \begin{cases} \exp(\sin(x+y)) - 1 & \text{if } (x,y) \in \Omega_1, \\ \sin(\pi(x+y)) & \text{if } (x,y) \in \Omega_2. \end{cases} \tag{5.3}$$

The source function f and u_D are manufactured by the exact solution. The diffusion coefficient has been defined to be $\rho_1 = \pi$ and $\rho_2 = 1$ and note that it holds $[\![u]\!]|_F = 0$ as well $[\![\rho\nabla u]\!]|_F \cdot n_F = 0$ for the normal flux on F. In this example, we investigate the convergence rates in case of utilizing B-spline spaces of degree $k = 3$ and the gap is a complex domain having the same shape as in Example 3. We solve the problem for $\lambda = 1$, 2, 3 and $\lambda = 4$. In any test case, we artificially create the gap region by moving appropriately the control points which are related to the interface F. In Fig. 5(a), we plot the contours of u on the domains Ω_l and Ω_r in case of $d_g = 0.1875$. In Fig. 5(b), we plot the contours of u_h on the same domains Ω_l and Ω_r. The convergence rates are plotted in Fig. 5(c). As in previous tests, the convergence behavior for all λ tests confirm the theoretical rates presented in Table 1. For the cases of $\lambda = 1$, $\lambda = 2$ and $\lambda = 3$, we observe that the rates are not optimal because the large gap distance, $d_g = h^\lambda$, affects the optimal approximation -related to the B-spline degree- of the normal fluxes on $\partial\Omega_g$. On the other hand, we get optimal rates $r = 3$ for $\lambda = 4$, because in this case we have optimal approximation $\mathcal{O}(h^3)$ of the normal fluxes on $\partial\Omega$, see Lemma 3.1 and Theorem 4.1.

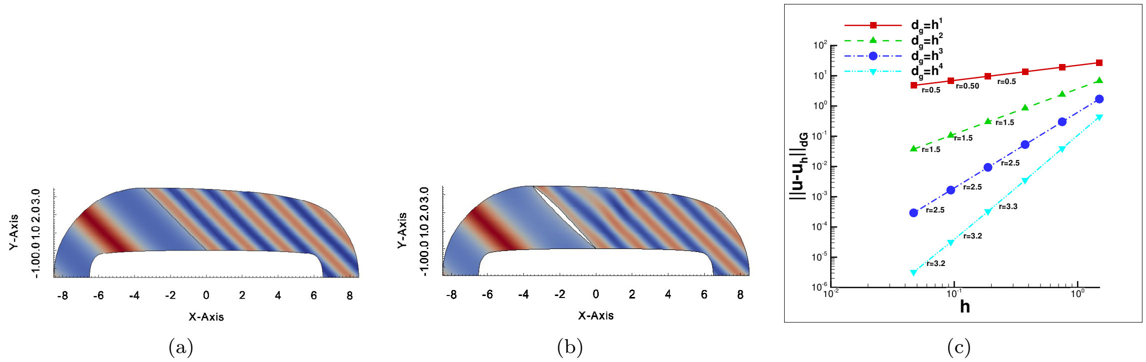

Figure 5: Example 4: third order, $k = 3$, B-spline space. (a) The contours of u on Ω_1 and Ω_2. (b) The contours of u_h on Ω_l and Ω_r computed for $d_g = 0.1875$ (c) Convergence rates r for the four values of λ.

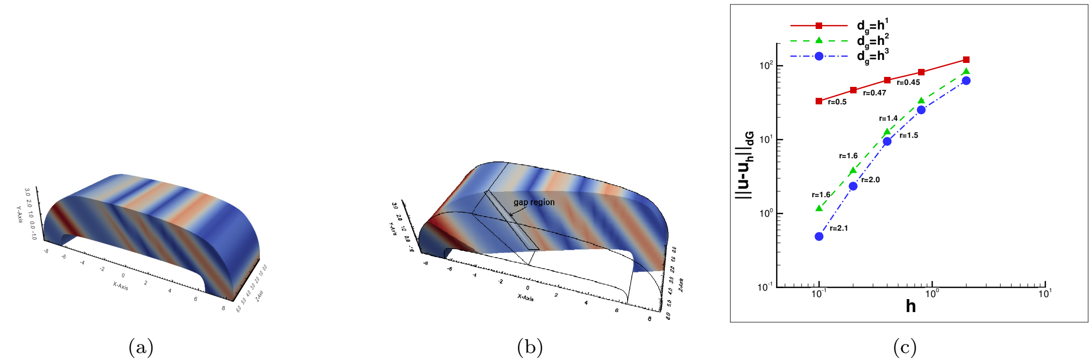

Figure 6: Example 5, $\Omega \subset \mathbb{R}^3$: (a) The contours of u_h computed on Ω , (b) The contours of u_h computed on $\Omega \setminus \overline{\Omega}_g$ with $d_g = 0.1$, (c) Convergence rates r for the three values of λ.

5.2. *Three-dimensional numerical examples*

In the three-dimensional tests, the domain Ω has been constructed by a straight prolongation to the z-direction of the previous two-dimensional domain, see Fig. 2(a). The knot vector in z-direction is the same as in the y-direction, this means $\Xi_i^3 = \{0, 0, 0, 0.5, 1, 1, 1\}$ with $i = l, r$. The B-spline parametrizations of the two subdomains have been build by adding a third component to the control points that are listed in the first two rows in Table 2. The third component takes the following values $\{0, 3, 6\}$. Again, the gap region is artificially constructed by moving only the interior control points located at the interface $F = \{(x, y, z) : y + x = 0,\ 0 \leq z \leq 6\}$ into the normal n_F-direction.

Example 5, 3d test with $\rho_l \neq \rho_r$. Although the first 3d example is a simple extension of the previous two dimensional Example 3, it is still interesting to check the numerical rates. The exact solution is given by (5.2) and the set up of the problem is illustrated in Fig. 6. The test has been performed using matching meshes on F_l and F_r. The interface F is the $y + x = 0$ plane. In Fig. 6(a), we can see the contours of the solution u on both subdomains Ω_1 and Ω_2 without having a gap region. Note that the contours resemble the two-dimensional contours along any slice $z = constant$. In Fig. 6(b), we plot the contours of the solution u_h resulting from the solution of the problem in case of having a gap region with $d_g = 0.1$. We can clearly observe the similarities of the contours in Fig. 4(b) and in Fig. 6(b). Also, in Fig. 6(b), we show the shape of the gap as it appears on an oblique cut of the domain Ω. We have computed the convergence rates for three different values $\lambda = 1$, $\lambda = 2$ and $\lambda = 3$. The results of the computed rates are plotted in Fig. 6(c). We observe that all the rates are in agreement with the rates predicted by the theory and are similar to the rates of the two-dimensional test Example 3, see Fig. 4(c).

Example 6, non-convex gap. For the second numerical test in three-dimensions, the domain Ω is the same as in previous Example 5 with the same interface F of Ω_1 and Ω_2, see Fig. 6(a). We consider a manufactured problem, where the solution is $u(x, y, z) = \sin(\pi x/2)\sin(\pi y/8)$, and the diffusion coefficient is defined to be $\rho = 1$ everywhere. Here, we artificially created the gap region such that $\Omega_g \subset \Omega_2$, and $\Omega_1 \subset \Omega_l$, see Fig. 7(a). Note that for this example the gap is not a convex region as in the previous test

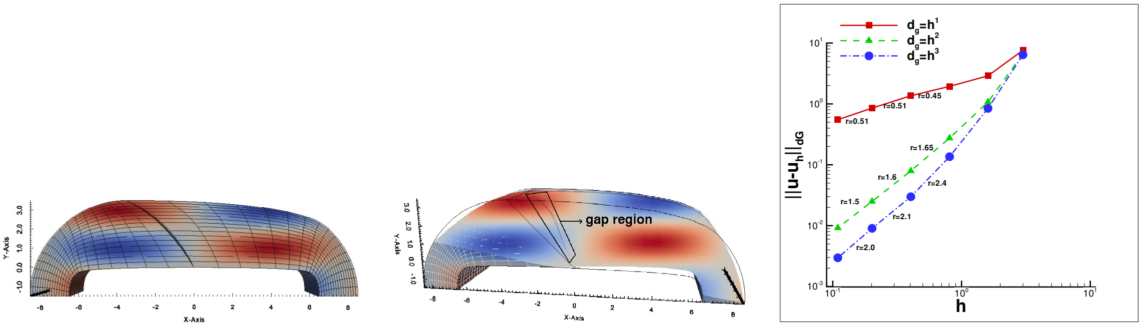

(a) (b) (c)

Figure 7: Example 6: (a) The contours of u on $\Omega \setminus \overline{\Omega}_g$ with $d_g = 0.15$ at $z = 3$, (b) The contours of u_h computed on $\Omega \setminus \overline{\Omega}_g$ with $d_g = 0.15$, (c) Convergence rates r for the different d_g sizes.

cases and this case is not covered by the description in Subsection 2.5. In particular, in all computations for this example, the two gap boundary parts F_l and F_r are not symmetrically located with respect to the original interface F. The problem has been solved performing three computations setting the parameter λ in the gap distance $d_g = h^\lambda$, equal to $\lambda = 1$, $\lambda = 2$ and $\lambda = 3$ correspondingly.

In Fig. 7(a), we can see the gap region, with $d_g = 0.15$ and the contours of the solution u on a $z = constant$ plane. The contours of the solution u_h computed on a non-matching decomposition with $d_g = 0.15$ are presented in Fig. 7(b). The contours are presented on a interior slice given by $z = 3$. We have computed the convergence rates r for the three different sizes d_g, obtained by the different values of λ. We plot our results in Fig. 7(c). We observe that the rates are approaching the expected values that have been mentioned in Table 1. Furthermore, we note that, for the case $d_g = h^3$, the rate tends to become optimal $r = 2$ and is in agreement with the rate predicted by the theory, see Table 1 and Theorem 4.1. Eventually, by this example with a non-convex gap, we show that the convergence rates are in agreement with the rates predicted by the theory.

Example 7, 4d test case. In this test case, we consider the model problem (2.3) in a domain $\Omega \subset \mathbb{R}^4$ with homogeneous diffusion coefficient $\rho = 1$ in the whole domain. The domain consists of two subdomains (hypercubes) Q_i, $i = 1, 2$ given by $Q_1 = [-1, 0] \times [0, 1]^3$ and $Q_2 = [0, 1] \times [0, 1]^3$ respectively. The common interface is the cube $Q_F = \{(x, y, z, w) : \{x = 0\} \times [0, 1]^3\}$. In Fig. 8(a), an illustration of the computational domain is presented and Q_F is depicted by red color. The exact solution is given by $u(x, y) = \sin(\pi y/2) \sin(\pi x/8) \sin(\pi z/2)$, the source term f and the boundary data u_D are manufactured by the exact solution. The domain is represented by second order B-Splines with knot vectors $\Xi_i^\iota = \{0, 0, 0, 0.5, 0.5, 1, 1, 1\}$ for $i \in \{1, 2\}$ and $\iota \in \{1, 2, 3, 4\}$ and the corresponding 81 control points for each patch, i.e., 3 control points along each dimension. In particular, we mark the only interior control point P_F of the common interface with the coordinates $P_F = (x = 0, y = 0.5, z = 0.5, w = 0.5)$. We create the gap by moving the control point P_F to the point $(x = d_g, y = 0.5, z = 0.5, w = 0.5)$. In Fig. 8(b), we illustrate the gap region in the interface cube. Note that in this test case the gap is a convex domain. The problem has been solved performing three computations setting the parameter λ in the gap distance $d_g = h^\lambda$, equal to $\lambda = 1$, $\lambda = 2$ and $\lambda = 3$ respectively. We have computed the convergence rates r for the three different sizes d_g, obtained by the different values of λ. In Fig. 8(c) we show the convergence rates of the error with respect the grid size. We observe that the rates are in agreement with the corresponding rates that have been found in the previous tests. Again, we observe that for the case $d_g = h^3$, the rate tends to get the optimal value $r = 2$ and is in agreement with the rate predicted by the theory, see Table 1 and Theorem 4.1. Finally, by this example with a convex gap $\Omega_g \subset \mathbb{R}^4$, we show that the convergence rates are in agreement with the rates predicted by the theory and this demonstrates the capability of our method to treat problems on decompositions with gaps even even in four-dimensional case.

6. Conclusions

In this article, we have developed and analyzed dG IgA methods for discretizing linear, second-order elliptic boundary value problems on volumetric patch decompositions with non-matching interface parametrizations, which include gap regions between the adjacent subdomains (patches). Starting from the original weak formulation, we derived a consistent variational problem on a decomposition without including the gap region. The unknown normal fluxes on the gap boundary were approximated via

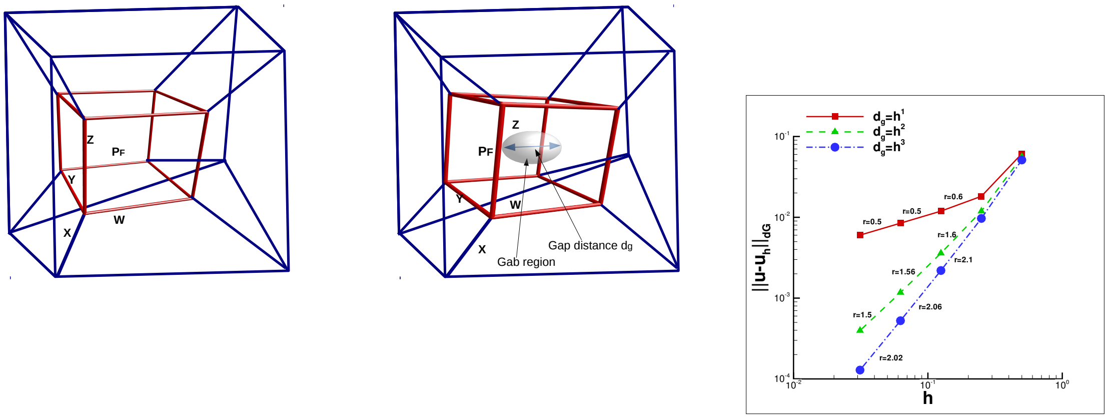

(a) (b) (c)

Figure 8: Example 7: (a) An illustration of the original domain, (b) An illustration of the computational domain with the gap region, (c) Convergence rates r for the different d_g sizes.

multi-directional Taylor expansions. The Taylor expansions were developed and were successfully used on simple and complex gap shapes. The approximations were adapted to the proposed dG IgA scheme, and the communication of the discrete solution of the adjacent subdomains was ensured. A priori error estimates in the dG-norm $\|.\|_{dG}$ were shown in terms of the mesh-size h and the gap distance d_g. The estimates were confirmed by solving several two-, three- and four-dimensional test problems with known exact solutions.

Acknowledgements

This work was supported by the Austrian Science Fund (FWF) under the grant NFN S117-03. This support is gratefully acknowledged. The authors wish to thank Prof. Ulrich Langer for his valuable comments during the preparation of the paper.

References

[1] R. A. Adams and J. J. F. Fournier. *Sobolev Spaces*, volume 140 of *Pure and Applied Mathematics*. ACADEMIC PRESS-imprint Elsevier Science, Amsterdam, Netherlands, second Edition edition, 2003.

[2] A. Apostolatos, R Schmidt, R. Wüchner, and K. U. Bletzinger. A Nitsche-type formulation and comparison of the most common domain decomposition methods in isogeometric analysis. *Int. J. Numer. Meth. Engng*, 97:473–504, 2014.

[3] E. Brivadis, A. Buffa, B. Wohlmuth, and L. Wunderlich. Isogeometric mortar methods. *Computer Methods in Applied Mechanics and Engineering*, 284(0):292 – 319, 2015. Isogeometric Analysis Special Issue.

[4] J. A. Cotrell, T.J.R. Hughes, and Y. Bazilevs. *Isogeometric Analysis, Toward Integration of CAD and FEA*. John Wiley and Sons, Sussex, United Kingdom, 2009.

[5] C. De-Boor. *A Practical Guide to Splines*, volume 27 of *Applied Mathematical Science*. Springer, New York, revised edition edition, 2001.

[6] A. Ern and J.-L. Guermond. *Theory and Practice of Finite Elements*, volume 159 of *Applied Mathematical Sciences*. Springer-Verlag New York, 2004.

[7] A. Falini, J. Špeh, and B. Jüttler. Planar domain parameterization with thb-splines. *Computer Aided Geometric Design*, vol:35-36:95–108, 2015.

[8] C. Hofer, U. Langer, and I. Toulopoulos. Discontinuous Galerkin Isogeometric Analysis of Elliptic Diffusion Problems on Segmentations with Gaps. RICAM-Technical and NFN-Technical Report No. 38, http://www.gs.jku.at/pubs/NFNreport38.pdf, Johann Radon Institute for Computational and Applied Mathematics, Austrian Academy of Sciences, 2015. available also at: http://arxiv.org/abs/1511.05715.

[9] J. Hoschek and D. Lasser. *Fundamentals of Computet Aided Geometric Design.* A K Peters, Wellesley, Massachusetts, 1993. Translated by L. Schumaker.

[10] B. Jüttler, M. Kapl, D.-M. Nguyen, Q. Pan, and M. Pauley. Isogeometric segmentation: The case of contractible solids without non-convex edges. *Computer-Aided Design*, 57:74–90, 2014.

[11] B. Jüttler, U. Langer, A. Mantzaflaris, S.E. Moore, and W. Zulehner. Geometry + Simulation Modules: Implementing Isogeometric Analysis. *PAMM*, 14(1):961–962, 2014.

[12] U. Langer, A. Mantzaflaris, St. E. Moore, and I. Toulopoulos. Multipatch discontinuous Galerkin isogeometric analysis. In B. Jüttler and B. Simeon, editors, *Isogeometric Analysis and Applications IGAA 2014*, Lecture Notes in Computer Science, Heidelberg, 2015. Springer. to appear, also available as RICAM Report no. 18 and at `arxiv.org/abs/1411.2478`.

[13] U. Langer and I. Toulopoulos. Analysis of multipatch discontinuous Galerkin IgA approximations to elliptic boundary value problems. RICAM Reports 2014-08, Johann Radon Institute for Computational and Applied Mathematics, Austrian Academy of Sciences, Linz, 2014. available also at: http://arxiv.org/abs/1408.0182.

[14] T. P. A. Mathew. *Domain Decomposition Methods for the Numerical Solution of Partial Ddifferential Equations.* Lecture Notes in Computational Science and Engineering. Springer-Verlag, Berlin Heidelberg, 2008.

[15] D.-M. Nguyen, M. Pauley, and B. Jüttler. Isogeometric segmentation. part ii: On the segmentability of contractible solids with non-convex edges. *Graphical Models*, 76:426–439, 2014.

[16] V. P. Nguyen, P. Kerfriden, M. Brino, S. P. A. Bordas, and E. Bonisoli. Nitsche's method for two and three dimensional NURBS patch coupling. *Computational Mechanics*, 53(6):1163–1182, 2014.

[17] M. Pauley, D.-M. Nguyen, D. Mayer, J. Speh, O. Weeger, and B. Jüttler. The isogeometric segmentation pipeline. In B. Jüttler and B. Simeon, editors, *Isogeometric Analysis and Applications IGAA 2014*, Lecture Notes in Computer Science, Heidelberg, 2015. Springer. to appear, also available as Technical Report no. 31 at http://www.gs.jku.at.

[18] M. Ruess, D. Schillinger, A. I. Özcan, and E. Rank. Weak coupling for isogeometric analysis of non-matching and trimmed multi-patch geometries. *Computer Methods in Applied Mechanics and Engineering*, 269(0):46 – 71, 2014.

[19] L. L. Schumaker. *Spline Functions: Basic Theory.* Cambridge, University Press, third Edition edition, 2007.